Journal Pre-proofs

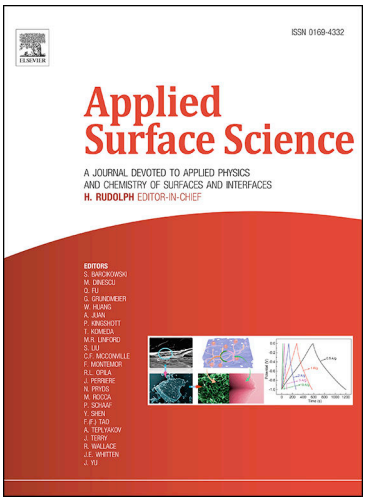

Full Length Article

Improving MgO/Fe Insulator-Metal Interface Structure through Oxygen-Precoating of Fe(001)

Nana K. M. Nazriq, Peter Krüger, Toyo Kazu Yamada

PII: S0169-4332(23)00304-5
DOI: https://doi.org/10.1016/j.apsusc.2023.156628
Reference: APSUSC 156628

To appear in: *Applied Surface Science*

Received Date: 21 December 2022
Revised Date: 27 January 2023
Accepted Date: 29 January 2023

Please cite this article as: N. K. M. Nazriq, P. Krüger, T. Kazu Yamada, Improving MgO/Fe Insulator-Metal Interface Structure through Oxygen-Precoating of Fe(001), *Applied Surface Science* (2023), doi: https://doi.org/10.1016/j.apsusc.2023.156628

Improving MgO/Fe Insulator-Metal Interface Structure through Oxygen-Precoating of Fe(001)

Nana K. M. Nazriq[1], Peter Krüger[1,2], and Toyo Kazu Yamada[1,2*]

1. Department of Materials Science, Chiba University, 1-33 Yayoi-Cho, Inage-ku, Chiba 263-8522, Japan.

2. Molecular Chirality Research Centre, Chiba University, 1-33 Yayoi-cho, Inage-ku, Chiba 263-8522, Japan.

Author Information,

Corresponding Author: Toyo Kazu Yamada *E-mail: **toyoyamada@faculty.chiba-u.jp**

Version 2023.1.28

Highlights

* Controlled *p*(1×1) oxygen pre-coating of Fe(001) drastically improves MgO film growth.

* Upon oxygen pre-coating, the MgO island size is increased by a factor of 10.

* Atomically-flat high-quality insulating MgO islands contain only few atomic defects.

* MgO islands also work as an electronic decoupling layer from the metal substrate.

Abstract

We grew atomically flat and electronically uniform MgO island terraces on a Fe(001) whisker substrate precoated by $p(1\times1)$ oxygen monolayer film. This interface engineering process increased about 10 times the size of MgO islands compared to the size of MgO islands directly grown on Fe(001), showing that the interface oxygen monolayer plays an essential role in MgO growth. Importantly, each squared-shape atomically flat MgO island includes only a few atomic defects, which provides high-quality insulating layers. Further, the MgO islands have an electronic decoupling functionality from the metal substrate. Surface morphology and local electronic structures were studied using a home-built ultrahigh vacuum scanning tunneling microscopy (STM) at a temperature of 5 K.

Keywords: magnesium oxide, iron, oxygen coating, scanning tunneling microscopy, phthalocyanine, organic molecule

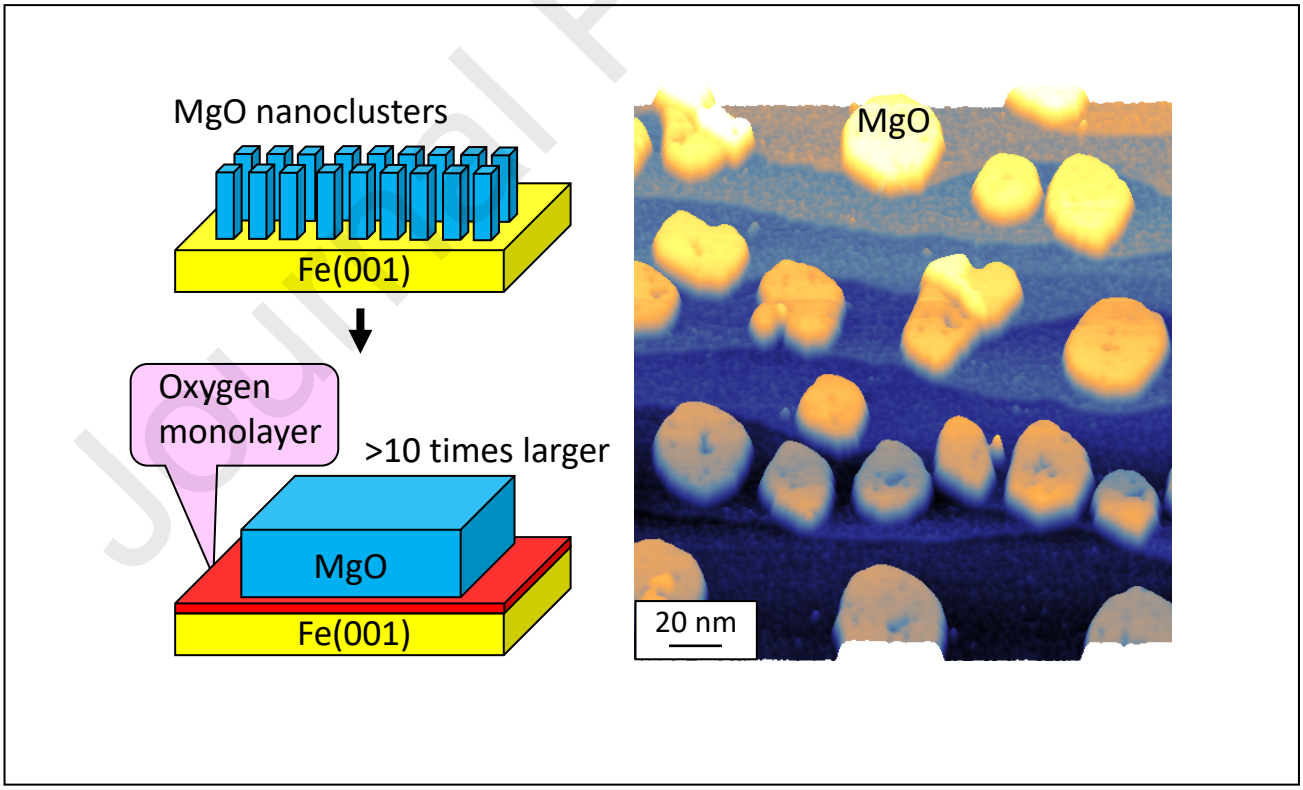

1. Introduction

A remarkable aspect of using the insulator films is their extremely high spin filter effect. Especially, the Fe/MgO(001) interface provided the theoretically predicted TMR values of 1000% [1,2] and the experimental TMR values of 200-600% at room temperature[3–6]. Thus Fe/MgO has been widely used as a tunnel magnetoresistance (TMR) head in a hard disk drive (HDD) and finds applications in magnetoresistive random access memory (MRAM). These large TMR values are generated by the realization of an atomically flat interface between Fe and MgO films. The cross-section view of atomically-resolved transmission electron microscopy images through the Fe/MgO(001) films showed atomically precise stacking of the MgO atomic layers on the Fe(001) film [3,4].

However, there is a problem with the reversed MgO/Fe interface, because, on the Fe(001) substrate, MgO grows as islands in the Volmer-Weber (VW) mode [7–9]. Therefore, MgO nanoclusters with a diameter of a few nanometers are obtained instead of a flat film. Small MgO nanocluster growth was also observed on the (001) surface of bcc molybdenum [10].

In this study, we introduced an ordered $p(1\times1)$ oxygen monolayer film at the interface between the MgO islands and Fe(001) whisker substrate [11–19]. This interface engineering drastically modified the MgO growth. It successfully increased the MgO island size to 10 times larger than MgO islands grown directly on Fe(001) and produced regularly shaped atomically flat and electronically uniform MgO nanoislands. This oxygen precoating weakens the bonding between adsorbed MgO atoms and the substrate Fe(001), enhancing the thermal diffusion of the Mg and O atoms. The diffusing atoms were trapped by the descending steps, forming nucleation. Other deposited Mg and O atoms were trapped by the nuclei, and the MgO island size increased until the MgO island reached another ascending step. The growth and electronic structures of the MgO islands were studied by using a home-built ultrahigh vacuum (UHV) scanning tunneling microscopy (STM) and scanning tunneling spectroscopy (STS) setup at a cryogenic temperature of 5 K [20–23].

Another important role of using such an atomically flat insulating surface with a thickness of several monolayers is an electronic decoupling functionality from its substrate, which allows direct visualization of free-standing electronic structures of adsorbents on a solid-state surface [24–35]. When adsorbed on noble metal substrates, NaCl and MgO films with a thickness of 2-4 monolayers (MLs)

follow the Frank-van der Merwe (FM) layer-by-layer growth mode and atomically flat insulating terraces with a 20-100 nm size can be achieved. These insulating surfaces have been widely used to investigate quantum spin states of isolated 3d/4f transition metal atoms or nodal planes of molecular orbitals of single organic molecules[36–38]. Herein we also demonstrate the electronic decoupling ability of the MgO islands grown on Fe(001)- $p(1\times1)$O using single organic CuPc molecules.

2. Methods

2.1 Home-built low-temperature UHV STM setup.

The experiment was performed with a home-built low-temperature STM at 5 K under UHV. The setup consists of the introduction, preparation, and analytical chambers with the base pressure below 10^{-8} Pa[20–23]. A UHV cryostat (CryoVac) including an outer liquid nitrogen tank (8 liters) and inner helium tank (4 liters) is docked on the analytical chamber. The STM was placed at the center of the analytical chamber thermally contacted with the cryostat. Heat radiation from the analytical chamber to the STM was cut with two cylindrical cooling shields, which maintained the STM temperature of 5 K for 40 h using 4 liters of liquid helium.

2.2 STM / STS measurements.

STM and scanning tunneling spectroscopy (STS) measurements were performed with a combined Nanonis SPM controller and software. The topographic images were obtained in a constant current mode. The obtained STM data were analyzed using WSxM 5.0 Develop 10.0 software[39] and Gwyddion 2.56. STS was done by measuring tunneling current as a function sample bias voltage ($I(V)$) at each pixel position in an STM topographic image (feedback-off grid mode). Differential conductance ($\mathrm{d}I/\mathrm{d}V$) curves, which are proportional to sample local density of states (LDOS), were obtained using WSxM 5.0 Develop 10.0 software[39] via numerical differentiation of $I(V)$ by the sample bias voltage (V).

2.3 Fabrication of W tip.

STM tips were fabricated from polycrystalline W and Mo wires with a diameter of 0.3 mm (purity 99.95 %) via electrochemical etching using KOH aq.[40] as well as the flame-etching process[41,42], and subsequently transferred into the UHV preparation chamber. Then, the tip apex was flashed at 2000 K to exclude oxide layers[40]. The cleaned tip was again transferred to the UHV analytical chamber without breaking UHV and set into the STM using a wobble stick.

2.4 Fe(001) preparation (see Supplementary Information, Fig.S1 and Fig. S3).

A Fe(001) single crystal whisker, which was grown via chemical vapor deposition[12,14], was cleaned by repeated cycles of Ar^+ sputtering (+0.8 kV, + 0.80 μA) at 820 K. The cleaned surface was checked by STM /STS, which showed atomically-flat terraces with a wide width of 50-100 nm and the Fe(001) 3*d* surface state peak at +0.2 eV in the d*I*/d*V* curves[12,15,18,43,44]. Low energy electron diffraction (LEED) spots showed the bcc(001) four-fold symmetry.

2.5 Fe(001)-p(1 ×1)O preparation (see Supplementary Information, Fig.S3).

The Fe(001)-*p*(1×1)O surface was prepared in the preparation chamber by exposing the clean Fe(001) surface to the oxygen gas of about 2 Langmuir (60 sec, 4.0×10^{-6} Pa) while maintaining the substrate temperature at 300 K. Then the sample was annealed up to 850 K for 15 min. STM topographic image showed a clear *p*(1×1) structure (see Supplementary Information, Fig.S3), where dark spots correspond to the oxygen atom position [8,13,19]. This oxygen monolayer coating prevents further oxidization and interface roughening.

2.6 Ultrathin MgO / Fe(001)-p(1 ×1)O preparation (see Supplementary Information, Fig.S2 and Fig.S3).

The Fe(001)-*p*(1×1)O surface was exposed again to the oxygen gas (60 s, 1.0×10^{-6} Pa) in the preparation chamber, and Mg atoms were deposited from the evaporator (AEV-3, AVC Co., Ltd.) at the sample temperature of 750 K (see Supplementary Information, Figs. S2 and S3). STM images showed growth of atomically-flat ultrathin squared-shaped nanoislands with a terrace width of about 40 nm and a uniform height of about 1 nm. Fe(001)-*p*(1×1)O terraces were still observed between the islands.

2.7 CuPc singles molecule deposition.

Although the CuPc molecule evaporation took place in the UHV chamber at room temperature condition, the sample was precooled at 5 K before the evaporation. CuPc was set in a crucible with a heat of 553 K. During the evaporation, the chamber pressure went up to 3.1×10^{-7} Pa. We spent three hours degassing and opened the shutter shortly only 3-5 seconds for deposition.

2.8 DFT calculation.

Density functional theory (DFT) calculations of CuPc molecules, either free or on MgO, were performed using the projector-augmented wave method as implemented in the VASP package [45,46]. The structures were optimized using the PBE exchange-correlation functional together with Grimme's DFT-D3 van der Waals corrections. The cut-off energy was set to 400 eV. We have modelled the CuPc/MgO system with a MgO substrate of two atomic layers. The coordinates of the lower layer are fixed to the bulk structure (with theoretical lattice constant a = 0.4208 nm) and the upper layer was fully relaxed. For the CuPc monolayer on MgO, we use a 5 × 5 supercell with 50 atoms per MgO layer and a 2 × 2 × 1 Monkhorst-Pack k-point mesh.

After structural optimization with the PBE functional, the electronic structure of the system was recalculated using the hybrid HSE06 functional[47,48]. The density of states plots in Fig. 4 correspond to the HSE functional which was found to provide a good description of the electronic state of CuPc [49]. Hybrid functionals also give much better band gap values than pure DFT functionals such as PBE. As a check, we also optimized the structure of the free CuPc molecule using HSE and found that the electronic structure changes between the PBE-optimized and the HSE-optimized molecule are negligible.

3. Results and Discussion

3.1 Growth of large atomically-flat MgO islands.

First, a Fe(001)-whisker single crystal, which was grown via chemical vapor deposition[12,14], was cleaned by repeated cycles of Ar^+ sputtering (+0.8 kV, + 0.80 μA) at 820 K. Then, at the final cycle, we maintained the sample temperature 820 K for 5-10 min after the sputtering, which increased the size of the Fe(001) terraces and cooled down to ~300 K for 15 min. Subsequently, the sample was transferred without breaking UHV to the STM cooling shield (~100 K) and waited about 3 hours. Finally, it was set into STM operated at 5 K (Methods and Supplementary Information, Fig. S1)[12,13,16,50–52]. Figure 1a shows an STM topographic image obtained on the Fe(001) surface, where several atomically-flat terraces are observed. The STS d*I*/d*V* curve measured on this surface indicates a 3*d* surface state peak at +0.2 eV[12,15,16], identifying the bcc-Fe(001).

It is known that Mg has a very low surface energy of 790 mJ/m^2 compared to the surface energy of Fe: 2550 mJ/m^2. [53] Therefore, when Mg films are grown directly on Fe(001) they follow the layer-by-layer FM mode as shown in Supplementary Information, Fig. S2. The surface energy of MgO (~1500 mJ/m^2)[54] is also much lower than that of Fe and so a layer-by-layer growth mode was expected for MgO, too. However, the direct growth of MgO on Fe(001) produced a rough surface. Figure 1b shows an STM topographic image obtained on the Fe(001) surface after Mg deposition in the oxygen atmosphere (~2×10^{-6} Pa). The whole surface was coated by 1-3 nm size nanoclusters, similar to previous studies [9].

This experimental evidence means that the MgO growth on Fe(001) is determined not only by thermodynamic stability, i.e. differences in surface energy, but also by kinetic aspects. The rough surface of MgO/Fe(001) in Fig. 1b was obtained by depositing Mg on Fe(001) in the oxygen atmosphere. In contrast, here the substrate Fe(001) was first exposed to oxygen at 300 K and then Mg was deposited in oxygen atmosphere. In previous experiments, we found that all Fe(001) terraces were covered by disordered oxide patches after the oxidization at 300 K, producing a rough surface[13]. If a similar oxidization process occurred during the MgO growth on Fe(001), because of the interface roughening, plenty of atomic defects were generated. These could trap the thermally diffused MgO,

resulting in and many nucleation sites, which leads to the growth of many independent MgO nanoislands of small size.

Therefore, if one first pre-coats the Fe(001) surface by an ordered oxygen monolayer with preserving an atomically-flat interface (less atomic defects), adsorbed MgO can thermally diffuse on the surface, which leads to a larger island. A ball-and-stick model is shown in Fig. 1c, where the adsorbed Mg and O atoms have thermally diffused on the surface. Once they are trapped, nucleation can occur, and subsequently, island growth starts. Previous studies reported an atomic layer distance of 0.143 nm in bulk bcc-Fe(001), while the distance at the interface changes to 0.17 nm and 0.21 nm between Fe and FeO, and FeO and MgO, respectively [55].

In order to use the oxygen passivation effect as depicted in the model in Fig. 1c, the Fe(001) surface was covered by one monolayer oxygen film by introducing oxygen gas of about 2 Langmuir (60 sec, 4.0×10^{-6} Pa) while maintaining the substrate temperature at 300 K. Then the sample was annealed up to 850 K for 15 min. In our previous study of temperature control of Fe-oxide growth on Fe(001)[13], only the Fe(001) oxidization at a substrate temperature of 300 K with a subsequent post-annealing to 850 K for 15 min produced the p(1×1) ordered oxygen coating film on Fe(001). Other conditions generated Fe_3O_4 (magnetite) nanoislands. Figure 1c shows an STM topographic image obtained after the oxidization of the Fe(001) surface. Several atomically-flat terraces were observed, while here all surface was covered by oxygen atoms by following the bcc(001) p(1×1) structure (dark spots in the inset in Fig. 1c). This oxygen coating changed the electronic structure of the surface as shown in the dI/dV curve in the inset in Fig. 1c, where the Fe(001) 3d surface state peak at +0.2 eV is quenched and a broad shoulder peak around +1 eV could be observed, in agreement with the previously reported Fe(001)- p(1×1)O structure. [13,19]

Then, we deposited MgO. The Fe(001)-p(1×1)O surface was exposed again to the oxygen gas (60 s, 1.0×10^{-6} Pa) in the preparation chamber. The magnesium (Mg) rod was evaporated in UHV (see Supplementary Information, Fig. S2), and the Mg atoms were oxidized in the UHV chamber by introducing the oxygen gas (2×10^{-6} Pa) and MgO atoms were adsorbed on the O/Fe(001) surface at the sample temperature of 750 K.

Figure 1d-h shows STM/STS results obtained on the Fe(001)-p(1×1)O surface after the Mg deposition at 750 K in oxygen gas dozing condition (2×10^{-6} Pa). The island growth was controlled by the Mg deposition time (t). Figure 1d-f shows STM topographic images obtained after t = 5 s, 60 s, and 120 s, respectively, at a sample bias of >3 V, well above the band gap. Height profiles along the arrows in Fig. 1d-f are shown in Fig. 1g, which clearly indicates that not only the size but also the height of the MgO islands increased.

At t = 5 s (Fig. 1d), all MgO islands are located along descending steps. This indicates that the diffused Mg and O atoms were first trapped at the descending steps and the island nucleation occurred. These islands had a non-uniform shape as depicted in lower panels in Fig. 1d, while the bcc(001) atomic lattices were locally observed. Another aspect is that the density of the growing islands was quite low: 18 / (100×100 nm^2) = 0.0018 nm^{-2}, indicating a low trapping rate of the diffused MgO atoms on O/Fe(001) compared to Fe(001). In Fig. 1g, the black line denotes the height profile along the arrow in Fig. 1d, which shows a corrugation on the island of ±50 pm. Such a small corrugation, much less than the atomic step height of 143 pm, could be caused by a nonuniform atomic arrangement inside the island.

The islands started to have a uniform regular shape from t = 60 s, namely a square shape following the bcc(001) square lattice as seen in Fig. 1e. The height profile along the arrow shows an atomically-flat surface on the MgO island (red line in Fig. 1g). A wide range STM topographic image shown in the lower panel in Fig. 1e indicates that the MgO island intensively grew at the descending steps. Therefore, the island density at the step area (σ_{step} = 10 / (200×100 nm^2) = 0.0005 nm^{-2}) is about 10 times higher than the density at the terrace area ($\sigma_{terrace}$ = 1 / (200×100 nm^2) = 0.00005 nm^{-2}). The size and the height of the islands are about 20×20 nm^2 and about 0.4 nm, respectively.

Figure 1f shows the oxygen pre-coated Fe(001) surface after the Mg deposition for t = 120 s. Compared to the surface at t = 60 s in Fig. 1e, the size of the island becomes about four times larger, about 40×40 nm^2. A line profile across one of the islands shows a height of about 0.8±0.1 nm (blue line in Fig. 1h). Although the size becomes larger, the island density remains the same: σ_{step} = 20 / (200×200 nm^2) = 0.0005 nm^{-2}, indicating an increase in island size.

The STM images in Fig. 1d-f also show the robustness and energetical stability of the Fe(001)-p(1×1)O surface since it is clear that there is no damage on the Fe(001)-p(1×1)O surface/interface after the MgO growth.

STM results of the MgO growth on Fe(001) (Fig. 1b) and Fe(001)-p(1×1)O (Fig. 1f) showed that oxygen passivation effect maintains the atomically-flat interface during the MgO growth at 750 K. Such a high temperature is required to suppress the Fe_3O_4 nanocluster generation in an oxygen atmosphere at lower temperatures[13]. There is a good contrast to the case of the insulating NaCl films directly grown on Fe(001) and O/Fe(001)[56]. The former and later follow the Stranski-Krastanov (SK) and FM mode, respectively, but the VW mode was never observed.

3.2 Electronic structures of insulating MgO islands.

The electronic structures of each pixel position on the surface were immediately measured by the STS method (see Methods). Namely, the STM tip was fixed on each pixel and measured the sample local density of states (LDOS) in the vicinity of the Fermi energy. The dI/dV curve is proportional to the LDOS: zero, positive, and negative bias sample voltages correspond to the Fermi energy, unoccupied, and occupied LDOS, respectively. Figure 1h shows dI/dV curves obtained on the oxygen-precoated Fe(001) surface (blue line) and the MgO island (red line). While the O/Fe(001) has LDOS peaks near the Fermi energy, the MgO has negligible LDOS (dI/dV ~ 0.0 nA/V) near the Fermi energy, indicating an insulating bandgap. A careful analysis of the electronic structures of these MgO islands is shown in Fig. 2.

We performed dI/dV curve measurements at each pixel position in the topographic image of Fig. 2a, where six MgO islands are observed. A simultaneously obtained dI/dV map at +2.45 V in Fig. 2b clearly shows a darker contrast for the MgO islands compared to the O/Fe(001) substrate. Since the brighter-darker contrast in dI/dV maps denotes higher and lower LDOS, respectively, it indicates that MgO could have a wide bandgap. Bulk MgO is an insulator with a large bandgap of 7.8 eV and a dielectric constant of 9.8[7–9,57,58]. All MgO nanoislands in the dI/dV map clearly show identical dark contrast, indicating that they also have a large gap. dI/dV curves corresponding to the four MgO nanoislands in Fig. 2a are shown in Fig. 2d, such that cyan, blue, red, and green colors denote each

island. All nanoislands have a bandgap of about 2.9 eV between -2.0 eV and +0.9 eV. This gap value is comparable to the previously reported gap width of 2.5 eV at two monolayers and 3.6 eV at six monolayers of MgO films on Fe(001) [7]. The dI/dV curve obtained on the substrate terrace is shown as a dashed line in Fig. 2d; it shows no bandgap.

Because of the large difference in the differential conductivity between the MgO islands and the substrate O/Fe(001), the apparent height (d_z) of the MgO islands from the substrate changes at different bias voltages. Fig. 2e shows that the MgO islands have a height of 0.18±0.02 nm within the gap. The height of the MgO nanoisland started to increase from 0.9 V, which is just above the bandgap, as d_z = 0.30±0.02 nm at +1 V, 0.62±0.02 nm at +2 V, and 1.00±0.04 nm at +4 V.

Although the apparent height of the MgO islands varies as a function of the sample bias voltage, the height obtained at +4 V, which is d_z ~ 1 nm, could represent the real height of the MgO islands as dI/dV values of the MgO islands and the substrate are comparable above +3 V (Fig. 2d). Also, we could estimate the thickness of the MgO island using previous reported layer distances. The distance between the first MgO layer and the Fe(001)-p(1×1)O substrate is 0.253 nm and the distance between the subsequent MgO layers is 0.239 nm [55,59]. d_{MgO} can be estimated from the four MgO monolayer (ML) stacking: d_{MgO} = 0.253 + 0.239*3 = 0.97 nm ~ 1 nm. Additionally, we deposited about 1.4 MLs of Mg on the substrate to grow the MgO nanoislands (Supplementary Information, Figs. S2 and S3). However, the MgO nanoislands cover only about 30% of the surface. This means that the nanoisland could have a height of 1.4/0.3 ~ 4.6 ML.

It should be noted that five MgO islands in Fig. 2a were grown along the descending steps, but only one island (left-lower side) was grown across the step, which generated an irregularly shaped island. This irregularly shaped island appeared much brighter in the dI/dV map at +3.36 V in Fig. 2c, indicating different LDOS from other regularly shaped islands. Figures 2f shows a comparison between dI/dV curves of regularly (black dots) and irregularly (red dots) shaped islands. Since the irregularly shaped islands have a LDOS peak at +3.2 eV above the Fermi energy, this could be a cause of the bright appearance in the dI/dV map in Fig. 2c. A height profile along the arrow in Fig. 2a is shown in the inset in Fig. 2f. Because of the higher LDOS, the apparent height of the irregularly shaped island is observed as an about 0.1 nm higher island (the inset in Fig. 2f). Furthermore, magnified spectra showed an additional shoulder and about 0.7 eV shift of the valence band are observed near the Fermi energy

(right panel in Fig. 2f), while both islands have no LDOS near the Fermi energy. They are observed as darker regions in the d*I*/d*V* map at 16 mV (the inset in the right panel).

3.3 Atomic defects inside MgO islands.

The d*I*/d*V* map at +3.36 eV in Fig. 2c reveals another aspect of the regular-shaped islands. Inside the MgO islands, some dark spots exist, which indicates a different LDOS from the surroundings. The electronic structure inside the MgO island was carefully investigated by measuring simultaneously topographic image and d*I*/d*V* curves at each pixel position (STS grid mode), which provides 200 d*I*/d*V* maps between ±4 V. In Fig. 3a, d*I*/d*V* maps obtained at -4.0, -1.6, +3.5, and +4.0 V are shown. With careful checks of these d*I*/d*V* maps, we found two different types of spots, which are marked by red (defect No.1) and blue (defect No.2) arrows in Fig. 3a. In the d*I*/d*V* maps at negative bias voltages (-4.0 V and -1.6 eV), brighter spots (red arrows, defect No.1) appeared in the dark MgO island. However, in the positive bias voltages, other dark spots (blue arrows, defect No.2) appeared. d*I*/d*V* curves obtained at defects No.1 and No.2 are shown in Fig. 3b. It is clear that LDOS at defect No.2 and MgO are very similar, but the LDOS at No.1 defect is clearly different, which has almost no bandgap but the LDOS decay exponentially to the Fermi energy. Series of d*I*/d*V* line profiles across the island clearly showed that the bright spot was visible at ±2 V (Supplementary, Fig. S4).

These indicate that defect No.1 could be an atomic defect, such as an atomic vacancy or misalignment of the local crystalline structure inside the island that significantly changes the electronic structure, causing in-gap states. However, defect No.2 seems to be the physisorbed impurity on the surface because of the tiny difference in the electronic structures. Therefore, such physisorbed impurities (defect No.2) could diffuse or desorb at room temperature. At the measurement temperature of 5 K, however, such processes are negligible and the impurities can clearly be observed in the STM image as dark spots.

Thus, atomic defects that significantly modify the electronic structure of MgO islands are rare, only about three in one MgO island, meaning that the defect concentration is much lower than 1%, thus providing uniform LDOS.

3.4 Electronic decoupling of adsorbed molecules from the metal substrate by MgO island

Here we show that when organic molecules are adsorbed on the MgO islands, the adsorbed molecules are well decoupled from the metal substrate such that their electronic structure is close to that of the gas phase free molecules. Thus, the large MgO islands obtained here by O-precoating of Fe(001) provide an efficient electronic decoupling layer which allows visualizing the molecular orbitals using STS.

Figure 4 shows Cu-phthalocyanine (CuPc) molecules deposited on the MgO nanoislands and the O/Fe(001) substrate terraces. Figure 4a shows a wide-range STM topographic image, where three MgO islands surrounded by the dotted curves were observed. It should be noted that nodal planes of the individual CuPc single molecules were clearly observed only on the MgO islands, which is actually clear evidence that the MgO islands grown on O/Fe(001) has an ability to decouple the electronic interaction from the metallic substrate. In contrast, the CuPc molecules adsorbed on the O/Fe(001) terrace were hardly identified as individual molecular shapes due to the direct electronic interaction with the metallic substrate.

Figure 4b shows a dI/dV spectrum obtained on the single CuPc molecule on MgO. The molecular nodal planes are clearly visible in the dI/dV maps around the HOMO (-1 eV) and LUMO (+2 eV) position. Between HOMO and LUMO peaks, dI/dV spectrum shows no differential conductivity (dI/dV ~ 0 pA/V), indicating a gap and a decoupling from the metallic Fe(001) substrate. These STM observations are in good agreement with STM results obtained on phthalocyanines adsorbed on insulating NaCl films[27,28,33,34].

In the present CuPc/MgO/O/Fe(001) system, the HOMO peak is located around -1 eV, while the LUMO peak is hidden in the conduction band of the substrate MgO/O/Fe. Note that in the case of CuPc/NaCl/Ag(111), HOMO and LUMO peaks were found at -2.4 eV and +0.9 V[60], and for CuPc/NaCl/Cu(111) at -2.2 eV and +1 V [61], respectively. The about 1 eV higher HOMO energy of CuPc/MgO/O/Fe(001) indicates that the charge transfer mechanism is different from the CuPc/NaCl/noble metal systems.

We have performed DFT calculations for the free CuPc molecule and for a CuPc monolayer on MgO. The PBE exchange-correlation functional was used for structural optimization and the HSE hybrid functional for the electronic state calculation, see the Methods section for further computational details.

We tested two adsorption sites, one with the Cu atom over Mg and one with Cu over O, which is shown in Fig. 4. This structure is more stable by 0.145 eV per molecule. The CuPc molecule is 0.30 ± 0.01 nm above the MgO substrate. The molecular is a little bent and the Cu atom relaxes slightly out of the molecular plane towards the substrate by 0.01 nm (with respect to the N atoms). Such a relaxation may be expected from the attractive Coulomb interaction between the Cu^{2+} ion and nearest neighbour O^{2-} ion on the substrate.

The calculated density of states (DOS) of free CuPc and CuPc/MgO are shown in Figs 4c and 4d, respectively. As the Fe substrate was not taken into account in the calculation, the exact position of the Fermi-level between HOMO and LUMO could not be determined theoretically. Therefore, we have shifted the DOS rigidly such as to align the HOMO peak with the experimental one. The HSE functional gives a HOMO-LUMO gap of 1.8 eV in reasonable agreement with experiment.

Importantly, it is seen that the HOMO-LUMO gap does not change upon adsorption on MgO. This result fully confirms the experimental observation that the electronic structure of the adsorbed CuPc is close to that of the free molecule, i.e. the molecule can be electronically decoupled from the metal substrate by insertion of a MgO film.

4. Conclusions

In summary, we have demonstrated that regularly-shaped and electronically uniform insulating MgO islands can be grown on a Fe(001) whisker substrate by inserting the interface $p(1\times1)$ oxygen monolayer film, which drastically increased the MgO island size by a factor of 10, compared to MgO islands grown directly on Fe(001). This interface engineering restricts the trapping probability of the adsorbed Mg and O atoms by Fe(001) and thus enhances adatom diffusion. The MgO island nucleated near the descending steps of the substrate. After nucleation, more Mg and O atoms accumulated at the nucleation site and the size of the islands increased until they reached other ascending steps. The regularly-shaped islands have identical LDOS with a gap of 2.9 eV and contain only a few atomic defects. However, when the MgO island grew after crossing the substrate step, irregularly-shaped islands were formed with different LDOS. Finally, it was demonstrated that the atomically-flat MgO island surface breaks the electronic coupling between adsorbed CuPc molecules and the metal substrate, such that the CuPc molecular orbitals could be clearly visualized.

CRediT authorship contribution statement

Nana Nazriq: Conceptualization, Methodology, Validation, Analysis, Investigation, Writing – original draft. **Peter Krüger:** Validation, Analysis, Calculation, Validation. **Toyo Kazu Yamada:** Conceptualization, Methodology, Validation, Analysis, Investigation, Writing – review & editing, Supervision, Project administration, Funding acquisition.

Declaration of Competing Interest

The authors declare that they have no known competing financial interests or personal relationships that could have appeared to influence the work reported in this paper.

Acknowledgments

This work was supported by JSPS KAKENHI Grant Numbers 17K19023 and the Murata Science Foundation. We thank Mr. Yuji Nonaka, Mr. Sakaguchi, and Ms. Kumi Kobayashi for their assistance at the early stage of the experiments. We acknowledge Dr. Lukas Gerhard (Institute for Quantum Materials and Technologies, Karlsruhe Institute of Technology, Germany) and Dr. Eiichi Inami (School of Systems Engineering, Kochi University of Technology, Japan) for the fruitful discussion.

Appendix A. Supplementary material

The Supporting Information is available.

Figures S1-S5 give additional experimental information.

Figure S1: Cleaning process of the Fe(001) whisker single crystal surface.

Figure S2: Magnesium evaporation control using quartz crystal microbalance and flux monitor, and STM study of 1.4 ML Mg / O / Fe(001).

Figure S3: STM/STS study of 1.4 ML Mg / O / Fe(001).

Figure S4: Line profiles of the STS dI/dV maps at various bias voltages across a defect in the regularly-shaped MgO island on O/Fe(001).

Figure S5. DFT calculated DOS results of free-standing CuPc and CuPc adsorbed on MgO surface.

References

(1) Butler, W. H.; Zhang, X.-G.; Schulthess, T. C.; MacLaren, J. M. Spin-Dependent Tunneling Conductance of Fe | MgO | Fe Sandwiches. *Phys. Rev. B* **2001**, *63* (5), 054416. https://doi.org/10.1103/PhysRevB.63.054416.

(2) Mathon, J.; Umerski, A. Theory of Tunneling Magnetoresistance of an Epitaxial Fe/MgO/Fe(001) Junction. *Phys. Rev. B* **2001**, *63* (22), 220403. https://doi.org/10.1103/PhysRevB.63.220403.

(3) Parkin, S. S. P.; Kaiser, C.; Panchula, A.; Rice, P. M.; Hughes, B.; Samant, M.; Yang, S.-H. Giant Tunnelling Magnetoresistance at Room Temperature with MgO (100) Tunnel Barriers. *Nat. Mater.* **2004**, *3* (12), 862–867. https://doi.org/10.1038/nmat1256.

(4) Yuasa, S.; Nagahama, T.; Fukushima, A.; Suzuki, Y.; Ando, K. Giant Room-Temperature Magnetoresistance in Single-Crystal Fe/MgO/Fe Magnetic Tunnel Junctions. *Nat. Mater.* **2004**, *3* (12), 868–871. https://doi.org/10.1038/nmat1257.

(5) Choi, J.-Y.; Lee, D.; Baek, J.-U.; Park, J.-G. Double MgO-Based Perpendicular Magnetic-Tunnel-Junction Spin-Valve Structure with a Top Co2Fe6B2 Free Layer Using a Single SyAF [Co/Pt]n Layer. *Sci. Rep.* **2018**, *8* (1), 2139. https://doi.org/10.1038/s41598-018-20626-4.

(6) Ikeda, S.; Hayakawa, J.; Ashizawa, Y.; Lee, Y. M.; Miura, K.; Hasegawa, H.; Tsunoda, M.; Matsukura, F.; Ohno, H. Tunnel Magnetoresistance of 604% at 300K by Suppression of Ta Diffusion in CoFeB/MgO/CoFeB Pseudo-Spin-Valves Annealed at High Temperature. *Appl. Phys. Lett.* **2008**, *93* (8), 082508. https://doi.org/10.1063/1.2976435.

(7) Klaua, M.; Ullmann, D.; Barthel, J.; Wulfhekel, W.; Kirschner, J.; Urban, R.; Monchesky, T. L.; Enders, A.; Cochran, J. F.; Heinrich, B. Growth, Structure, Electronic, and Magnetic Properties of MgO/Fe(001) Bilayers and Fe/MgO/Fe(001) Trilayers. *Phys. Rev. B* **2001**, *64* (13), 134411. https://doi.org/10.1103/PhysRevB.64.134411.

(8) Cattoni, A.; Petti, D.; Brivio, S.; Cantoni, M.; Bertacco, R.; Ciccacci, F. MgO/Fe(001) and MgO / Fe (001) − p (1 × 1) O Interfaces for Magnetic Tunnel Junctions: A Comparative Study. *Phys. Rev. B* **2009**, *80* (10), 104437. https://doi.org/10.1103/PhysRevB.80.104437.

(9) Dugerjav, O.; Kim, H.; Seo, J. M. Growth of a Crystalline and Ultrathin MgO Film on Fe(001). *AIP Adv.* **2011**, *1* (3), 032156. https://doi.org/10.1063/1.3642601.

(10) Benedetti, S.; Myrach, P.; di Bona, A.; Valeri, S.; Nilius, N.; Freund, H.-J. Growth and Morphology of Metal Particles on MgO/Mo(001): A Comparative STM and Diffraction Study. *Phys. Rev. B* **2011**, *83* (12), 125423. https://doi.org/10.1103/PhysRevB.83.125423.

(11) Venus, D.; Heinrich, B. Interfacial Mixing of Ultrathin Cr Films Grown on an Fe Whisker. *Phys. Rev. B* **1996**, *53* (4), R1733–R1736. https://doi.org/10.1103/PhysRevB.53.R1733.

(12) Yamada, T. K.; Yamagishi, Y.; Nakashima, S.; Kitaoka, Y.; Nakamura, K. Role of π − d Hybridization in a 300-K Organic-Magnetic Interface: Metal-Free Phthalocyanine Single Molecules on a Bcc Fe(001) Whisker. *Phys. Rev. B* **2016**, *94* (19), 195437. https://doi.org/10.1103/PhysRevB.94.195437.

(13) Yamada, T. K.; Sakaguchi, Y.; Gerhard, L.; Wulfhekel, W. Temperature Control of the Growth of Iron Oxide Nanoislands on Fe(001). *Jpn. J. Appl. Phys.* **2016**, *55* (8S1), 08NB14. https://doi.org/10.7567/JJAP.55.08NB14.

(14) Yamada, T. K.; Tamura, H.; Shishido, M.; Irisawa, T.; Mizoguchi, T. Surface Reconstruction of Clean Bcc-Fe{110}: A Quasi-Hexagonal Top-Layer with Periodic Height Modulation. *Surf. Sci.* **2009**, *603* (2), 315–319. https://doi.org/10.1016/j.susc.2008.11.010.

(15) Stroscio, J. A.; Pierce, D. T.; Davies, A.; Celotta, R. J.; Weinert, M. Tunneling Spectroscopy of Bcc (001) Surface States. *Phys. Rev. Lett.* **1995**, *75* (16), 2960–2963. https://doi.org/10.1103/PhysRevLett.75.2960.

(16) Bischoff, M. M. J.; Yamada, T. K.; Fang, C. M.; de Groot, R. A.; van Kempen, H. Local Electronic Structure of Fe(001) Surfaces Studied by Scanning Tunneling Spectroscopy. *Phys. Rev. B* **2003**, *68* (4), 045422. https://doi.org/10.1103/PhysRevB.68.045422.

(17) Bischoff, M. M. J.; Yamada, T.; Quinn, A. J.; van Kempen, H. Scanning Tunneling Microscopy and Spectroscopy Study on the Submonolayer Growth of Mn on Fe(). *Surf. Sci.* **2002**, *501* (1–2), 155–167. https://doi.org/10.1016/S0039-6028(01)01946-X.

(18) Yamada, T. K.; Bischoff, M. M. J.; Heijnen, G. M. M.; Mizoguchi, T.; van Kempen, H. Observation of Spin-Polarized Surface States on Ultrathin Bct Mn(001) Films by Spin-Polarized Scanning Tunneling Spectroscopy. *Phys. Rev. Lett.* **2003**, *90* (5), 056803. https://doi.org/10.1103/PhysRevLett.90.056803.
(19) Donati, F.; Sessi, P.; Achilli, S.; Li Bassi, A.; Passoni, M.; Casari, C. S.; Bottani, C. E.; Brambilla, A.; Picone, A.; Finazzi, M.; Duò, L.; Trioni, M. I.; Ciccacci, F. Scanning Tunneling Spectroscopy of the Fe (001) − p (1 × 1) O Surface. *Phys. Rev. B* **2009**, *79* (19), 195430. https://doi.org/10.1103/PhysRevB.79.195430.
(20) Nazriq, N. K. M.; Krüger, P.; Yamada, T. K. Carbon Monoxide Stripe Motion Driven by Correlated Lateral Hopping in a 1.4 × 1.4 Monolayer Phase on Cu(111). *J. Phys. Chem. Lett.* **2020**, *11* (5), 1753–1761. https://doi.org/10.1021/acs.jpclett.9b03645.
(21) Nemoto, R.; Krüger, P.; Putri Hartini, A. N.; Hosokai, T.; Horie, M.; Kera, S.; Yamada, T. K. Well-Ordered Monolayer Growth of Crown-Ether Ring Molecules on Cu(111) in Ultra-High Vacuum: An STM, UPS, and DFT Study. *J. Phys. Chem. C* **2019**, *123* (31), 18939–18950. https://doi.org/10.1021/acs.jpcc.9b03335.
(22) Inami, E.; Yamaguchi, M.; Yamaguchi, T.; Shimasaki, M.; Yamada, T. K. Controlled Deposition Number of Organic Molecules Using Quartz Crystal Microbalance Evaluated by Scanning Tunneling Microscopy Single-Molecule-Counting. *Anal. Chem.* **2018**, *90* (15), 8954–8959. https://doi.org/10.1021/acs.analchem.8b01118.
(23) Inami, E.; Shimasaki, M.; Yorimitsu, H.; Yamada, T. K. Room Temperature Stable Film Formation of π-Conjugated Organic Molecules on 3d Magnetic Substrate. *Sci. Rep.* **2018**, *8* (1), 353. https://doi.org/10.1038/s41598-017-18605-2.
(24) Schintke, S.; Messerli, S.; Pivetta, M.; Patthey, F.; Libioulle, L.; Stengel, M.; De Vita, A.; Schneider, W.-D. Insulator at the Ultrathin Limit: MgO on Ag(001). *Phys. Rev. Lett.* **2001**, *87* (27), 276801. https://doi.org/10.1103/PhysRevLett.87.276801.
(25) Mantilla, M.; Jedrecy, N.; Lazzari, R.; Jupille, J. Oxidation of Mg/Ag(111) Investigated Using Scanning Tunneling Microscopy: Towards Atomically Smooth MgO Nanostructures. *Surf. Sci.* **2008**, *602* (19), 3089–3094. https://doi.org/10.1016/j.susc.2008.07.043.
(26) Nakashima, S.; Yamagishi, Y.; Oiso, K.; Yamada, T. K. How Contacting Electrodes Affect Single π-Conjugated Molecular Electronic States: Local Density of States of Phthalocyanine Nanomolecules on MgO(001), Cu(111), Ag(001), Fe(001), and Mn(001). *Jpn. J. Appl. Phys.* **2013**, *52* (11R), 110115. https://doi.org/10.7567/JJAP.52.110115.
(27) Shin, H.-J.; Jung, J.; Motobayashi, K.; Yanagisawa, S.; Morikawa, Y.; Kim, Y.; Kawai, M. State-Selective Dissociation of a Single Water Molecule on an Ultrathin MgO Film. *Nat. Mater.* **2010**, *9* (5), 442–447. https://doi.org/10.1038/nmat2740.
(28) Wu, S. W.; Nazin, G. V.; Chen, X.; Qiu, X. H.; Ho, W. Control of Relative Tunneling Rates in Single Molecule Bipolar Electron Transport. *Phys. Rev. Lett.* **2004**, *93* (23), 236802. https://doi.org/10.1103/PhysRevLett.93.236802.
(29) Khajetoorians, A. A.; Wiebe, J.; Chilian, B.; Wiesendanger, R. Realizing All-Spin–Based Logic Operations Atom by Atom. *Science* **2011**, *332* (6033), 1062–1064. https://doi.org/10.1126/science.1201725.
(30) Myrach, P.; Nilius, N.; Freund, H.-J. Photon Mapping of Individual Ag Particles on MgO/Mo(001). *Phys. Rev. B* **2011**, *83* (3), 035416. https://doi.org/10.1103/PhysRevB.83.035416.
(31) Li, Z.; Schouteden, K.; Iancu, V.; Janssens, E.; Lievens, P.; Van Haesendonck, C.; Cerdá, J. I. Chemically Modified STM Tips for Atomic-Resolution Imaging of Ultrathin NaCl Films. *Nano Res.* **2015**, *8* (7), 2223–2230. https://doi.org/10.1007/s12274-015-0733-y.
(32) Leon, C. C.; Grewal, A.; Kuhnke, K.; Kern, K.; Gunnarsson, O. Anionic Character of the Conduction Band of Sodium Chloride. *Nat. Commun.* **2022**, *13* (1), 981. https://doi.org/10.1038/s41467-022-28392-8.
(33) Doležal, J.; Merino, P.; Redondo, J.; Ondič, L.; Cahlík, A.; Švec, M. Charge Carrier Injection Electroluminescence with CO-Functionalized Tips on Single Molecular Emitters. *Nano Lett.* **2019**, *19* (12), 8605–8611. https://doi.org/10.1021/acs.nanolett.9b03180.
(34) Repp, J.; Meyer, G.; Stojković, S. M.; Gourdon, A.; Joachim, C. Molecules on Insulating Films: Scanning-Tunneling Microscopy Imaging of Individual Molecular Orbitals. *Phys. Rev. Lett.* **2005**, *94* (2), 026803. https://doi.org/10.1103/PhysRevLett.94.026803.

(35) Steurer, W.; Gross, L.; Meyer, G. Local Thickness Determination of Thin Insulator Films via Localized States. *Appl. Phys. Lett.* **2014**, *104* (23), 231606. https://doi.org/10.1063/1.4883219.
(36) Fernandes, E.; Donati, F.; Patthey, F.; Stavrić, S.; Šljivančanin, Ž.; Brune, H. Adsorption Sites of Individual Metal Atoms on Ultrathin MgO(100) Films. *Phys. Rev. B* **2017**, *96* (4), 045419. https://doi.org/10.1103/PhysRevB.96.045419.
(37) Kawai, S.; Foster, A. S.; Canova, F. F.; Onodera, H.; Kitamura, S.; Meyer, E. Atom Manipulation on an Insulating Surface at Room Temperature. *Nat. Commun.* **2014**, *5* (1), 4403. https://doi.org/10.1038/ncomms5403.
(38) Singha, A.; Willke, P.; Bilgeri, T.; Zhang, X.; Brune, H.; Donati, F.; Heinrich, A. J.; Choi, T. Engineering Atomic-Scale Magnetic Fields by Dysprosium Single Atom Magnets. *Nat. Commun.* **2021**, *12* (1), 4179. https://doi.org/10.1038/s41467-021-24465-2.
(39) Horcas, I.; Fernández, R.; Gómez-Rodríguez, J. M.; Colchero, J.; Gómez-Herrero, J.; Baro, A. M. WSXM : A Software for Scanning Probe Microscopy and a Tool for Nanotechnology. *Rev. Sci. Instrum.* **2007**, *78* (1), 013705. https://doi.org/10.1063/1.2432410.
(40) Yamada, T. K.; Abe, T.; Nazriq, N. M. K.; Irisawa, T. Electron-Bombarded 〈110〉-Oriented Tungsten Tips for Stable Tunneling Electron Emission. *Rev. Sci. Instrum.* **2016**, *87* (3), 033703. https://doi.org/10.1063/1.4943074.
(41) Yamaguchi, T.; Inami, E.; Goto, Y.; Sakai, Y.; Sasaki, S.; Ohno, T.; Yamada, T. K. Fabrication of Tungsten Tip Probes within 3 s by Using Flame Etching. *Rev. Sci. Instrum.* **2019**, *90* (6), 063701. https://doi.org/10.1063/1.5085251.
(42) Goto, Y.; Suizu, R.; Noguchi, Y.; Yamada, T. K. Oxidative Vaporization Etching for Molybdenum Tip Formation in Air. *Appl. Surf. Sci.* **2021**, *542*, 148642. https://doi.org/10.1016/j.apsusc.2020.148642.
(43) Kosuge Y.; Yamada T. K. Spin-Polarized Scanning Tunneling Microscopy Study of Non-Collinear Magnetic Coupling in Layerwise Antiferromagnetic Mn(001) Ultra-Thin Films on Fe(001) due to Interface Roughening. *Vac. Surf. Sci.* **2020**, *63* (9), 459–464. https://doi.org/10.1380/vss.63.459.
(44) Schlickum, U.; Janke-Gilman, N.; Wulfhekel, W.; Kirschner, J. Step-Induced Frustration of Antiferromagnetic Order in Mn on Fe(001). *Phys. Rev. Lett.* **2004**, *92* (10), 107203. https://doi.org/10.1103/PhysRevLett.92.107203.
(45) Kresse, G.; Joubert, D. From Ultrasoft Pseudopotentials to the Projector Augmented-Wave Method. *Phys. Rev. B* **1999**, *59* (3), 1758–1775. https://doi.org/10.1103/PhysRevB.59.1758.
(46) Kresse, G.; Furthmüller, J. Efficient Iterative Schemes for *Ab Initio* Total-Energy Calculations Using a Plane-Wave Basis Set. *Phys. Rev. B* **1996**, *54* (16), 11169–11186. https://doi.org/10.1103/PhysRevB.54.11169.
(47) Heyd, J.; Scuseria, G. E.; Ernzerhof, M. Hybrid Functionals Based on a Screened Coulomb Potential. *J. Chem. Phys.* **2003**, *118* (18), 8207–8215. https://doi.org/10.1063/1.1564060.
(48) Krukau, A. V.; Vydrov, O. A.; Izmaylov, A. F.; Scuseria, G. E. Influence of the Exchange Screening Parameter on the Performance of Screened Hybrid Functionals. *J. Chem. Phys.* **2006**, *125* (22), 224106. https://doi.org/10.1063/1.2404663.
(49) Marom, N.; Hod, O.; Scuseria, G. E.; Kronik, L. Electronic Structure of Copper Phthalocyanine: A Comparative Density Functional Theory Study. *J. Chem. Phys.* **2008**, *128* (16), 164107. https://doi.org/10.1063/1.2898540.
(50) Yamada, T. K.; Bischoff, M. M. J.; Mizoguchi, T.; van Kempen, H. STM and STS Study of Ultrathin Mn Layers on Fe(). *Surf. Sci.* **2002**, *516* (1–2), 179–190. https://doi.org/10.1016/S0039-6028(02)02032-0.
(51) Yamada, T. K.; Bischoff, M. M. J.; Vázquez de Parga, A. L.; Mizoguchi, T.; van Kempen, H. Study of Fe/Mn/Fe Multilayers by Means of Scanning Tunneling Microscopy/Spectroscopy. *Surf. Sci.* **2004**, *558* (1–3), 201–210. https://doi.org/10.1016/j.susc.2004.04.004.
(52) Yamada, T. K.; Vazquez de Parga, A. L. Room Temperature Spin-Polarizations of Mn-Based Antiferromagnetic Nanoelectrodes. *Appl. Phys. Lett.* **2014**, *105* (18), 183109. https://doi.org/10.1063/1.4901047.
(53) Miedema, A. R.; de Châtel, P. F.; de Boer, F. R. Cohesion in Alloys — Fundamentals of a Semi-Empirical Model. *Phys. BC* **1980**, *100* (1), 1–28. https://doi.org/10.1016/0378-4363(80)90054-6.
(54) Zhang, D.-N.; Zhao, L.; Wang, J.-F.; Li, Y.-L. ELECTRONIC STRUCTURES AND THE STABILITY OF MgO SURFACE: DENSITY FUNCTIONAL STUDY. *Surf. Rev. Lett.* **2015**, *22* (03), 1550037. https://doi.org/10.1142/S0218625X15500377.

(55) Yu, B. D.; Kim, J.-S. *Ab Initio* Study of Ultrathin MgO Films on Fe (001) : Influence of Interfacial Structures. *Phys. Rev. B* **2006**, *73* (12), 125408. https://doi.org/10.1103/PhysRevB.73.125408.
(56) Tekiel, A.; Topple, J.; Miyahara, Y.; Grütter, P. Layer-by-Layer Growth of Sodium Chloride Overlayers on an Fe(001)-p(1 × 1)O Surface. *Nanotechnology* **2012**, *23* (50), 505602. https://doi.org/10.1088/0957-4484/23/50/505602.
(57) Heo, S.; Cho, E.; Lee, H.-I.; Park, G. S.; Kang, H. J.; Nagatomi, T.; Choi, P.; Choi, B.-D. Band Gap and Defect States of MgO Thin Films Investigated Using Reflection Electron Energy Loss Spectroscopy. *AIP Adv.* **2015**, *5* (7), 077167. https://doi.org/10.1063/1.4927547.
(58) Yan, L.; Lopez, C. M.; Shrestha, R. P.; Irene, E. A.; Suvorova, A. A.; Saunders, M. Magnesium Oxide as a Candidate High-κ Gate Dielectric. *Appl. Phys. Lett.* **2006**, *88* (14), 142901. https://doi.org/10.1063/1.2191419.
(59) Tusche, C.; Meyerheim, H. L.; Jedrecy, N.; Renaud, G.; Ernst, A.; Henk, J.; Bruno, P.; Kirschner, J. Oxygen-Induced Symmetrization and Structural Coherency in Fe / MgO / Fe (001) Magnetic Tunnel Junctions. *Phys. Rev. Lett.* **2005**, *95* (17), 176101. https://doi.org/10.1103/PhysRevLett.95.176101.
(60) Doležal, J.; Mutombo, P.; Nachtigallová, D.; Jelínek, P.; Merino, P.; Švec, M. Mechano-Optical Switching of a Single Molecule with Doublet Emission. *ACS Nano* **2020**, *14* (7), 8931–8938. https://doi.org/10.1021/acsnano.0c03730.
(61) Uhlmann, C.; Swart, I.; Repp, J. Controlling the Orbital Sequence in Individual Cu-Phthalocyanine Molecules. *Nano Lett.* **2013**, *13* (2), 777–780. https://doi.org/10.1021/nl304483h.

Figures / Figure captions

Figure 1

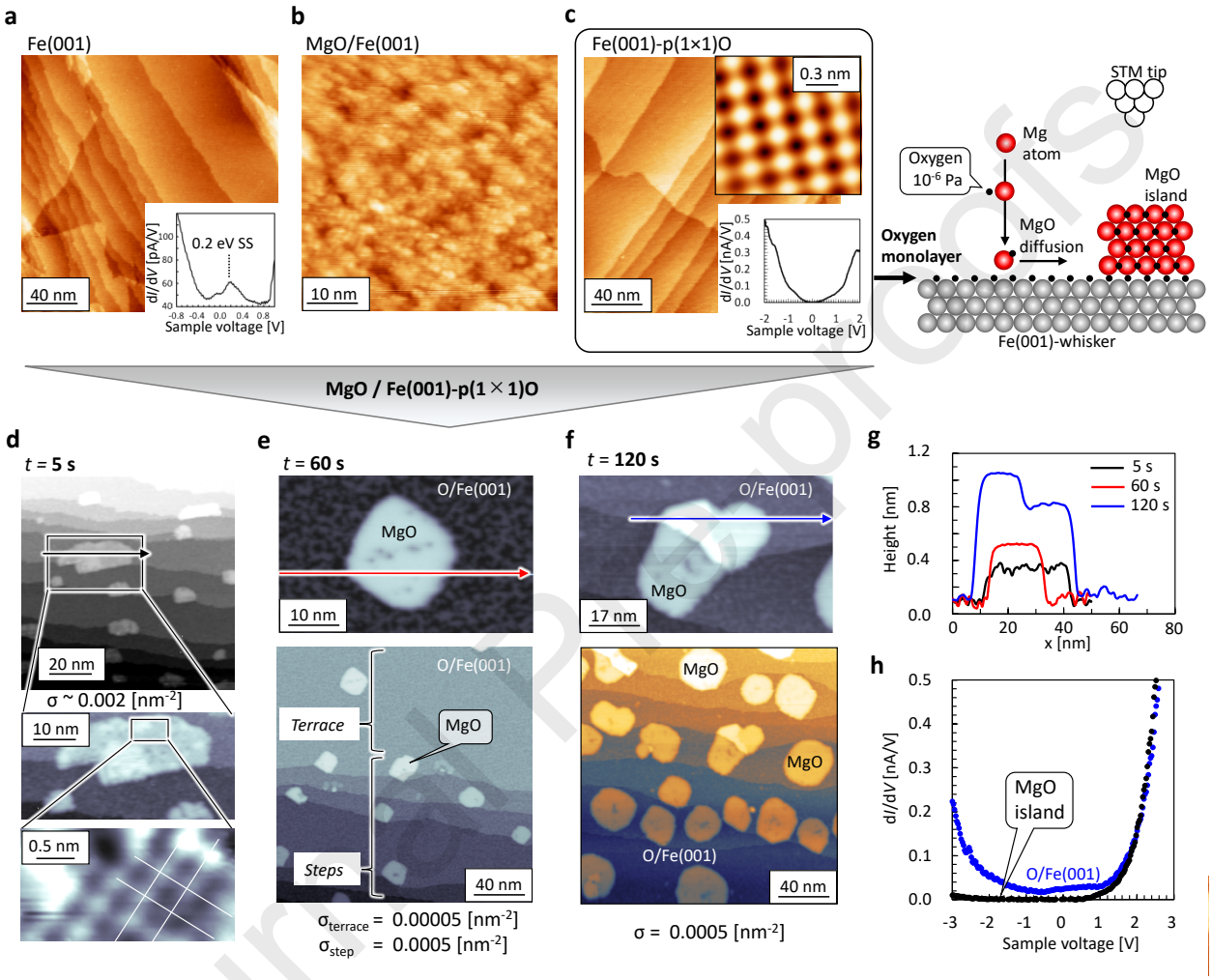

Figure 1. UHV-STM imaging at 5 K of MgO islands grown on Fe(001)-p(1×1)O substrate. (a-c) STM topographic images obtained on (a) the cleaned Fe(001) surface (200×200 nm^2, V_s = -1 V, I = 200 pA), (b) MgO nanoislands on Fe(001) (50×50 nm^2, V_s = 3.5 V, I = 50 pA), and (c) the oxygen-precoated Fe(001)-p(1×1)O surface (200×200 nm^2, V_s = -0.5 V, I = 200 pA). Inset in (a) shows the dI/dV spectrum obtained on the Fe(001) surface with a peak at 0.2 eV arising from the surface state present on the clean Fe(001) surface. Insets in (c) show an atomically-resolved image and the dI/dV curve of the Fe(001)-p(1×1)O lattice. Right panle in (c) denotes a side view of the spherical model. White, red, and grey spheres denote W, Mg, and Fe atoms, respectively. Black dots denote oxygen atoms. (d-h) STM/STS results obtained on the O/Fe(001) surface after Mg deposition for (d) 5 s, (e) 60 s, and (f) 120 s in oxygen atmosphere (10^{-6} Pa). (d) STM topographic images from top to down: 100×100 nm^2, 50×25 nm^2, 2.9×1.5 nm^2 (V_s = +3.0 V, I = 810 pA). (e) STM topographic images: higher panel 50×30 nm^2 and lower panel 200×200 nm^2 (V_s = +3.5 V, I = 950 pA). (f) STM topographic images: higher panel 80×50 nm^2 and lower panel 200×200 nm^2 (V_s = +3 V, I = 50 pA). (g) Height profiles along the black, red, and blue arrows in (d), (e), and (f), respectively. (h) dI/dV curves obtained on the Fe(001)-p(1×1)O substrate (blue line) and the MgO island (black line).

Figure 2

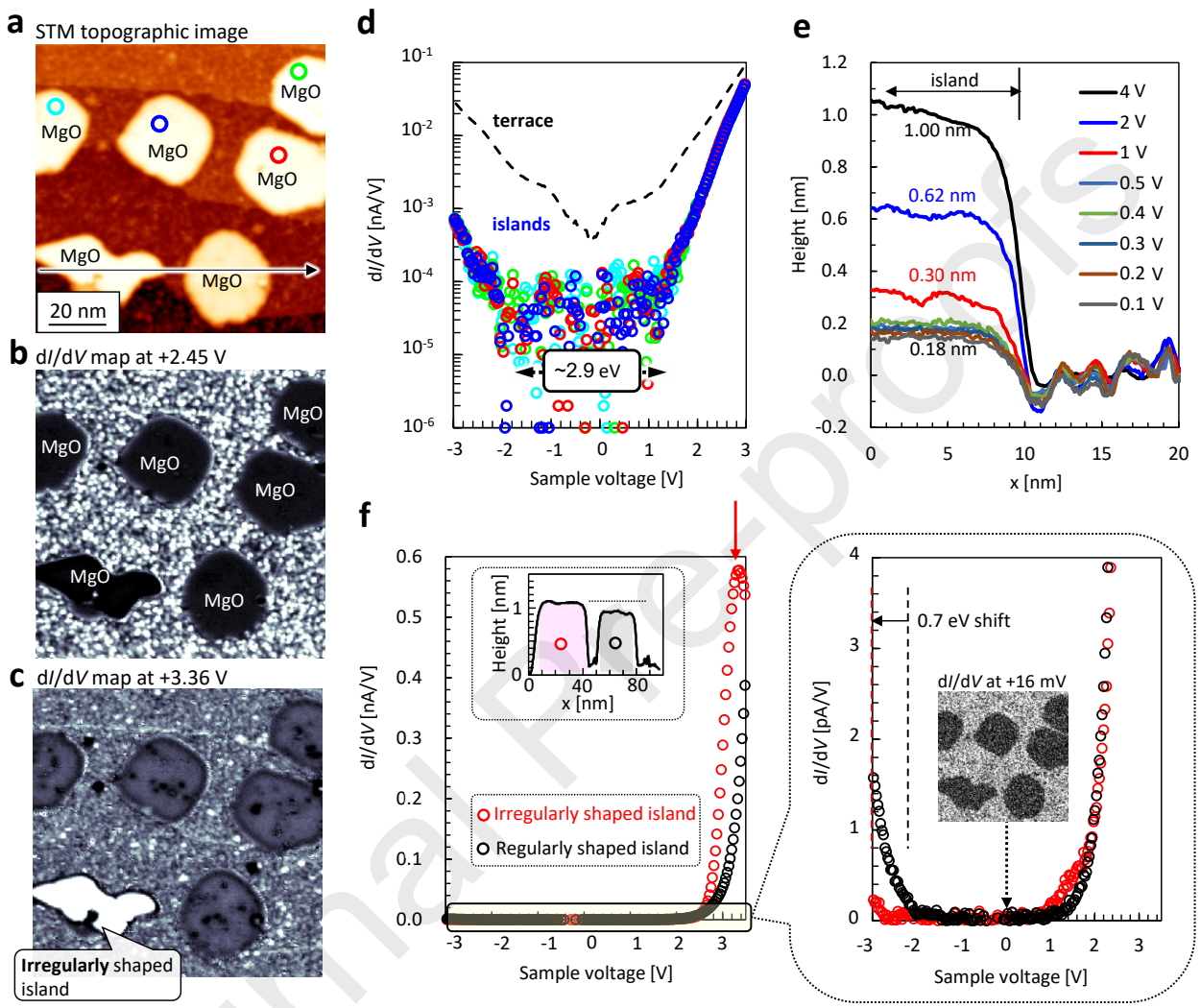

Figure 2. Electronic structure of MgO islands grown on Fe(001)-$p(1\times1)$O substrate. (a) STM topographic image: 100×100 nm^2, V_s = +4.0 V, I = 1 nA, and (b, c) simultaneously obtained dI/dV maps at (b) +2.45 V and (c) +3.36 V. (d) dI/dV curves obtained on the four MgO islands marked by cyan, blue, red and green circles in (a), indicating a bandgap of about 2.9 eV (from -2 V to +0.9 V). The dI/dV curve obtained on the substrate is shown as a dashed line. (e) Apparent height (d_z) of the observed MgO islands at different sample voltages. (f) dI/dV curves obtained on the regularly (black) and the irregularly (red) shaped MgO nanoislands. The right panel denotes the magnified spectra. The inset shows dI/dV map within the gap at +16 mV.

Figure 3

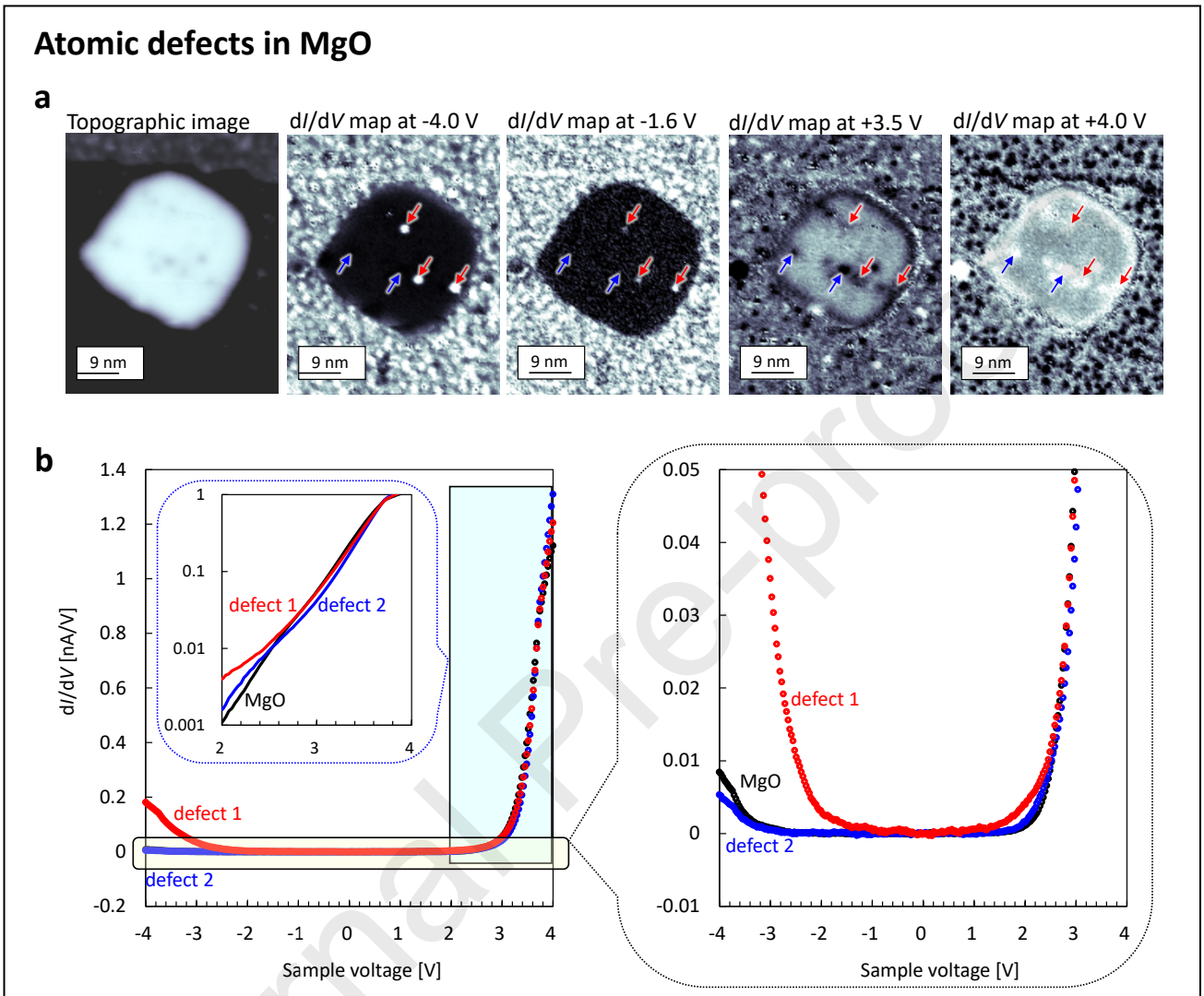

Figure 3. Atomic defects in the regularly shaped MgO island grown on Fe(001)-*p*(1×1)O substrate. (a) STM topographic image: 45×56 nm^2, V_s = +4.0 V, I = 1 nA, and simultaneously obtained dI/dV maps at -4.0 V, -1.6 V, +3.5 V, and +4.0 eV. Red and blue arrows denote two kinds of defects: defect 1 and 2, respectively. (b) dI/dV curves obtained at the MgO surface (black dots), defect 1 (red dots), and defect 2 (blue dots) positions. The right panel denotes magnified spectra.

Figure 4

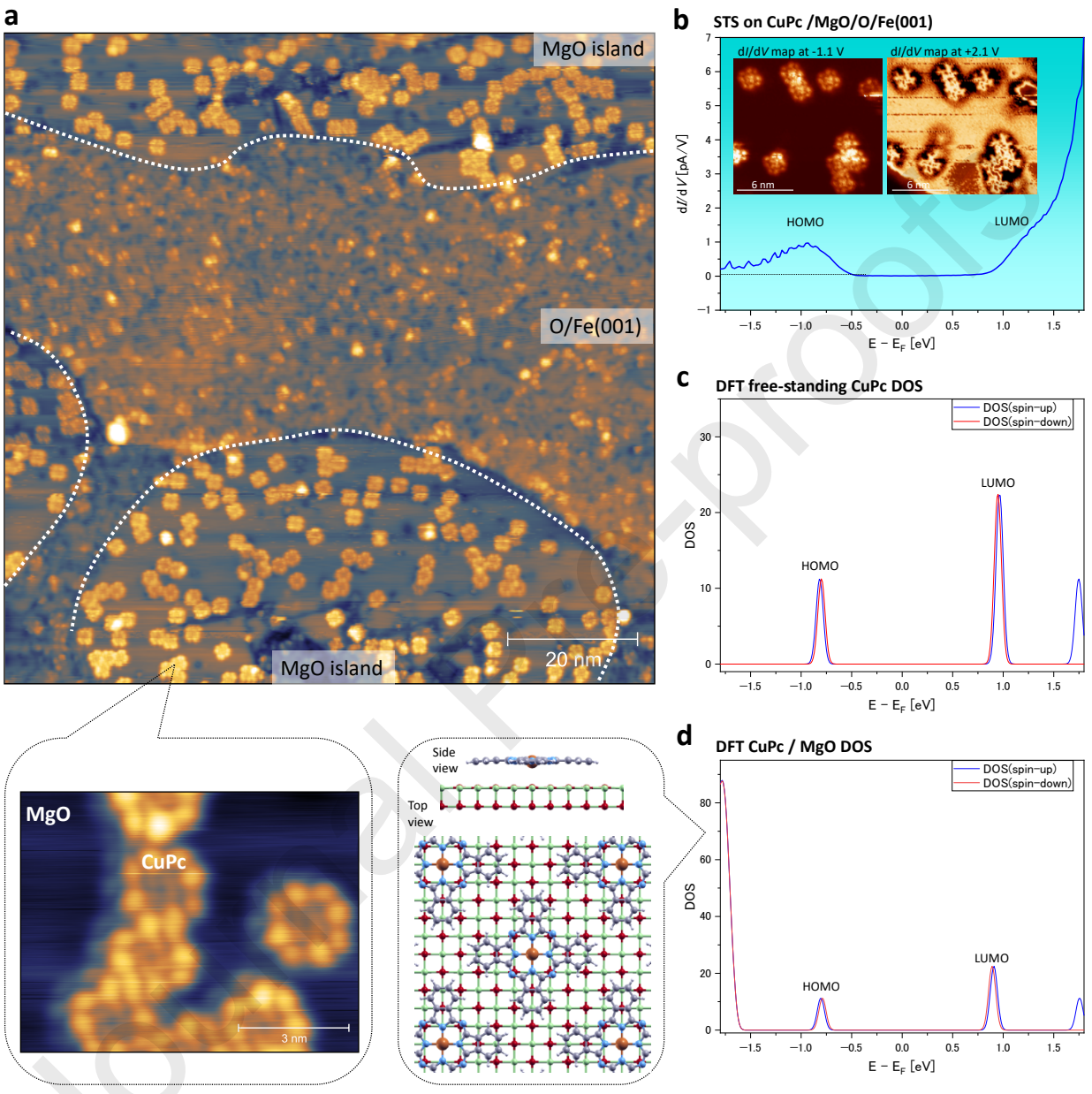

Figure 4. UHV-STM imaging at 5 K of Cu-phthalocyanine (CuPc) molecules adsorption on MgO islands grown on Fe(001)-p(1×1)O substrate. (a) STM topographic image: 100×100 nm^2, V_s = -1.0 V, I = 100 pA. The inset shows the magnified image of CuPc at -2 V. (b) Upper panel: dI/dV curve obtained on single CuPc molecules. dI/dV values of about 0 pA/V means a gap, indicating an electronic decoupling from the metallic Fe(001) substrate. Insets denote dI/dV maps around -1 V and +2 V. Lower panel: DFT calculated density of states (DOS) of free-standing CuPc.

A. Namiki, N. Nakashima, K. Yoshihara, Fluorescence quenching due to the electron transfer. Indole-chloromethanes in rigid ethanol glass, J. Chem. Phys. 71(2) (1979) 925–930. https://doi.org/10.1063/1.438383.